







# Investigation of Congo Red Photodegradation Catalyzed by MOFs ZIF-67@SiO<sub>2</sub> Composite Under Sunlight

Evi Maryanti <sup>1,\*</sup>, Wulan Aprilia Syafitri <sup>2</sup>, Eka Angasa <sup>1</sup>, Nor Kartini Abu Bakar <sup>3</sup>, Kiky Corneliasari Sembiring <sup>4</sup>, Grandprix T.M. Kadja <sup>5,6,7</sup>

<sup>1</sup> Department of Chemistry, Faculty of Mathematics and Natural Science, University of Bengkulu, W.R Supratman, Kandang Limun, 38371, Bengkulu, Indonesia; [evi.maryanti@unib.ac.id](mailto:evi.maryanti@unib.ac.id) (E.M.); [eka.angasa@unib.ac.id](mailto:eka.angasa@unib.ac.id) (E.A.);

<sup>2</sup> Undergraduate Student of Department of Chemistry, Faculty of Mathematics and Natural Science, University of Bengkulu, W.R Supratman, Kandang Limun, 38371, Bengkulu, Indonesia; [wulanaprilaa4@gmail.com](mailto:wulanaprilaa4@gmail.com) (W.A.);

<sup>3</sup> Department of Chemistry, Faculty of Sciences, Universiti Malaya Kuala Lumpur-50603, Malaysia; [kartini@um.edu.my](mailto:kartini@um.edu.my) (N.K.);

<sup>4</sup> Research Center for Chemistry, National Research and Innovation Agency (BRIN), B.J. Habibie Science and Technology Area, South Tangerang 15314, Indonesia; [kiky001@brin.go.id](mailto:kiky001@brin.go.id) (K.C.);

<sup>5</sup> Division of Inorganic and Physical Chemistry, Institut Teknologi Bandung, Jl. Ganesha No. 10, Bandung, 40132, Indonesia; [grandprix.thomryes@itb.ac.id](mailto:grandprix.thomryes@itb.ac.id) (G.T.);

<sup>6</sup> Research Center for Nanosciences and Nanotechnology, Institut Teknologi Bandung, Jl. Ganesha No. 10, Bandung 40132, Indonesia

<sup>7</sup> Center for Catalysis and Reaction Engineering, Institut Teknologi Bandung, Jl. Ganesha No. 10, Bandung 40132, Indonesia

\* Correspondence: [evi.maryanti@unib.ac.id](mailto:evi.maryanti@unib.ac.id);

Received: 10.03.2025; Accepted: 10.05.2025; Published: 9.08.2025

**Abstract:** Metal-organic frameworks (MOFs) ZIF-67 and ZIF-67@SiO<sub>2</sub> composites were synthesized using a solvothermal method combined with *in situ* impregnation at varying SiO<sub>2</sub> concentrations (4%, 8%, and 12% by weight). Phase identification, crystal structure, morphology, particle size, texture properties, and microporosity of the materials were analyzed using XRD, FTIR, Raman spectroscopy, SEM-EDS, and BET techniques. The photodegradation performance of Congo red in an aqueous solution was evaluated by measuring adsorption capacity and degradation percentages for ZIF-67 and ZIF-67@SiO<sub>2</sub> composites with different SiO<sub>2</sub> concentrations and contact times. Phase and crystal structure analyses confirmed the formation of the crystalline ZIF-67 phase, with variations in crystallinity. FTIR and Raman spectroscopy indicated that the addition of silica did not damage the ZIF-67 structure. Surface morphology analysis revealed that ZIF-67 and its composite particles exhibited a rhombic dodecahedron shape, with particle size increasing as silica content increased. The ZIF-67@SiO<sub>2</sub> (8%) composite demonstrated the highest photodegradation performance for Congo red under sunlight, achieving a degradation percentage of 72.79% and following pseudo-second-order adsorption kinetics.

**Keywords:** metal-organic framework; ZIF-67; congo red; silica; photodegradation.

© 2025 by the authors. This article is an open-access article distributed under the terms and conditions of the Creative Commons Attribution (CC BY) license (<https://creativecommons.org/licenses/by/4.0/>), which permits unrestricted use, distribution, and reproduction in any medium, provided the original work is properly cited. The authors retain copyright of their work, and no permission is required from the authors or the publisher to reuse or distribute this article, as long as proper attribution is given to the original source.

## 1. Introduction

Colorants are essential chemicals in various industries; however, they are currently a major source of contamination in aquatic environments [1]. More than 60% of the most widely used synthetic dyes globally are azo dyes, with approximately 10-15% being non-recyclable and subsequently discharged into the environment [2-4]. One of the organic dyes commonly

used in industries is Congo red (CGR), a secondary diazo dye that is toxic, carcinogenic, and mutagenic to aquatic organisms [5-7]. CGR is extensively utilized in the textile industry, papermaking, plastics, paints, wood, and other sectors. Classified as a hazardous organic dye, CGR exhibits high toxicity even at low concentrations and, therefore, must not be indiscriminately discharged into the environment due to its significant ecological risks [8]. Consequently, an effective and environmentally friendly technique is needed to remove dyes, particularly CGR [9]. Various chemical and physical methods have been developed for this purpose, including biological oxidation [10], adsorption [11], photocatalysis [12,13], and ion exchange [14]. Among these methods, photocatalysis stands out as one of the most promising due to its great efficiency, affordability, and operational simplicity.

An ideal catalyst for degradation should be stable under acidic or basic conditions, highly porous, cost-effective, easy to apply, and simple to retrieve [14-16]. The effectiveness of catalytic methods depends on factors such as selectivity, kinetics, rapid mass transfer, high specific surface area, low-cost preparation, flexibility, and recyclability [17-19]. Porous materials, such as metal-organic frameworks (MOFs), have emerged as promising catalysts [20]. MOFs are materials with pores composed of metal nodes and organic ligands as linkers, offering unique properties such as a large surface area and tunable bandgap energy [21-24]. To enhance MOF efficiency, researchers leverage their flexibility in modifying pore structure, specific surface area, surface active sites, crystallinity, topology/morphology, and chemical-physical stability [25-30]. Zeolitic Imidazolate Frameworks (ZIF)-67, a type of multifunctional MOF, has been applied in various domains, including photocatalysis [31,32], adsorption [33,34], sensors [35], gas storage, catalysis [26], and supercapacitors [36]. ZIF-67 possesses a large surface area ( $SBET > 1700 \text{ m}^2/\text{g}$ ), providing abundant active sites [32].

In recent decades, numerous studies have attempted to enhance ZIF-67 efficiency through metal incorporation, post-synthetic metalation, functional group addition, mineralization, structure-directing agents, and carbon hybridization [37-39]. These efforts have resulted in composites with superior performance compared to unmodified ZIF-67. For example, Xuan *et al.* reported the synthesis of hydroxyapatite-modified ZIF-67 composites, exhibiting effective and selective uranium (IV) elimination from wastewater [40]. Similarly, ZIF-67/CNF/PANI composites synthesized via a hydrothermal method at room temperature have been used as electrochemical sensors [41]. Composite microspheres, such as ZIF-67/PES, have demonstrated potential applications in removing triarylmethane dyes [42]. Additionally, Singh *et al.* developed ZIF-67/PVA nanofibers with high potential for water treatment remediation [43]. Apart from metals and polymers, silica-rich minerals such as silica, zeolite, kaolin, and clay can be combined with MOFs to enhance their performance [44]. These silica-based materials are preferred due to their porous characteristics, high surface area, adjustable polarity based on surface charge density, and thermal and chemical stability [45,46]. For instance, Pawar *et al.* synthesized MOF@sepiolite composites, which exhibited perfect octahedral MOF morphology, excellent dispersion on the sepiolite surface, thermal stability, and efficient performance in degrading RhB dye [47]. Furthermore, MOF@clay composites synthesized via solvothermal methods demonstrated fast, efficient, and stable absorption performance in reducing organic pollutants [48]. Bentonite, when used as a supporting material for ZIF-8, yielded bentonite/ZIF-8 composites with high stability for the photodegradation of congo red dye [49].

The synthesis of MOFs ZIF-67 composites using silica-based minerals has not been widely reported. Silica is a compound with excellent chemical stability and mechanical properties, offering significant benefits when combined with MOFs to enhance their properties and performance. Silica not only provides structured support for MOF materials but also improves material stability through hydrophobic interactions and covalent bonding. For instance, Sun *et al.* synthesized  $\text{SiO}_2@\text{ZIF-67}/\text{CNTs}$  composites, exhibiting good adsorption performance for methyl orange (112 mg/g) at low temperatures (5 °C). The calcined composite demonstrated a specific surface area of 1135 m<sup>2</sup>/g, as high-temperature calcination evaporates organic materials within the material, thereby increasing its porosity and ultimately enhancing its specific surface area [50]. Wang *et al.* explored MXene membranes modified with ZIF-67 and sepiolite. By utilizing the high porosity and active sites of ZIF-67, as well as the negative surface charge and hydrophilicity of sepiolite, the separation efficiency of the MXene membrane was significantly enhanced [51]. Recently, a hybrid nanostructure design based on ZIF-67 and silica was developed to produce yolk-shell structured  $\text{ZIF-67}@\text{SiO}_2$  nanocomposites. The study revealed that the specific surface area (SSA) of silica had a greater impact on improving energy storage performance (electrochemical properties) compared to the porosity properties of ZIF-67 [52].

In this research, in situ impregnation of mesoporous silica powder into MOFs ZIF-67 was performed using a solvothermal method, which was subsequently applied to remove Congo red dye pollutants. The addition of silica, characterized by larger pore sizes (mesopores), non-toxic and environmentally friendly properties, and high chemical and thermal stability, was expected to enhance the chemical and physical stability, as well as the catalytic and adsorption performance, of ZIF-67 in addressing environmental water pollutant dyes. The physicochemical characteristics of the resulting  $\text{ZIF-67}@\text{SiO}_2$  composite were analyzed using several instrumental techniques, including X-ray Diffraction (XRD), Fourier Transform Infrared Spectroscopy (FTIR), Raman Spectroscopy, Scanning Electron Microscopy-Energy Dispersive Spectroscopy (SEM-EDS), and N<sub>2</sub> adsorption-desorption isotherms with Brunauer-Emmett-Teller (BET) analysis. The photocatalytic activity of the composite was evaluated based on the variation in silica mass added to ZIF-67 and the contact time, using Ultraviolet-Visible Spectroscopy (UV-Vis) under direct sunlight radiation.

## 2. Materials and Methods

### 2.1. Materials.

$\text{Co}(\text{NO}_3)_2 \cdot 6\text{H}_2\text{O}$ , methanol, chloroform, and Congo red were purchased from Merck KGaA. 2-methylimidazole (2-MeIM) was purchased from Sigma-Aldrich, and silica powder was obtained from Unichem Specialty Chemicals (LLC). Distilled water (aquadest) was purchased from Brataco. All chemicals and solvents used in this study were of high quality and were used without further purification.

### 2.2. Synthesis of ZIF-67 and $\text{ZIF-67}@\text{SiO}_2$ composites.

The synthesis of ZIF-67 MOFs was adapted from the procedure by Saeed *et al.* with slight modifications [53]. ZIF-67 was synthesized using a metal-to-ligand molar ratio of 1:8 (mmol/mmol).  $\text{Co}(\text{NO}_3)_2 \cdot 6\text{H}_2\text{O}$  (1.436 g) was dissolved in 100 mL of methanol, and 2-methylimidazole (3.244 g) was dissolved in 100 mL of methanol in a separate container. The

$\text{Co}(\text{NO}_3)_2 \cdot 6\text{H}_2\text{O}$  solution was slowly added to a Duran bottle containing the 2-methylimidazole solution. The resulting mixture was stirred with a magnetic stirrer for 3 hours and left to stand for 24 hours at room temperature. The precipitate was separated using a centrifuge at 4000 rpm for 30 minutes and washed three times with methanol and once with chloroform. The product was then dried in an oven at 100 °C for 36 hours and further characterized.

The synthesis of the ZIF-67@SiO<sub>2</sub> composite followed the procedure for pure ZIF-67 synthesis, with the addition of SiO<sub>2</sub> prior to adding the  $\text{Co}(\text{NO}_3)_2 \cdot 6\text{H}_2\text{O}$  solution. SiO<sub>2</sub> was added to the mixture of 2-MeIM and SiO<sub>2</sub> in varying mass percentages of 4%, 8%, and 12% relative to the mass of pure ZIF-67. This step aimed to determine the optimal silica mass that would enhance the photocatalytic properties of the synthesized ZIF-67@SiO<sub>2</sub>. In previous research by Ediat *et al.* [54], ZIF-67 composites with MCM-41 were synthesized with mass percentages of 2.5%, 5%, and 10%. The study revealed a trend in which the adsorption capacity of the composite increased with higher mass percentages.

### 2.3. Photocatalytic degradation study.

Congo red (CGR) was used as the dye pollutant to evaluate the photocatalytic properties of ZIF-67 and ZIF-67@SiO<sub>2</sub>. Adsorption studies were performed in 30 mL vials containing 0.01 g of each catalyst mixed with 20 mL of CGR solution (initial concentration = 40 mg/L). The mixtures were stirred in the dark for 30 minutes to reach adsorption equilibrium. Samples were then centrifuged to separate the catalysts, and the CGR concentration was measured at 499 nm using UV-Vis spectroscopy. Subsequently, the samples were exposed to sunlight for 30, 60, 90, and 120 minutes. These time intervals were used to examine the degradation kinetics and to determine whether the degradation followed first-order, second-order, or complex kinetics. Time intervals also provided insights into the structural and functional stability of ZIF-67 before degradation began [55]. Periodic samples were centrifuged, and the final CGR concentration was determined. The percentage degradation of the pollutant was calculated using the following formula:

$$\% \text{ degradation} = \frac{C_o - C_e}{C_o} \times 100\% \quad (1)$$

**Notes:** Co and Ce are the initial and final CGR concentrations (mg/L), respectively.

The adsorption capacity (qt; mg/g) was calculated using the following formula:

$$qt = \frac{(C_o - C_e)V}{w} \quad (2)$$

**Notes:** Co and Ce are the initial and equilibrium CGR concentrations (mg/L), V is the solution volume (L), and w is the catalyst mass (g).

### 2.4. Characterization.

The crystal structures of all samples were characterized using X-ray diffraction (XRD) on a PANalytical X'Pert diffractometer with Cu-K $\alpha$  radiation at 40 kV and 30 mA, within a scanning range of  $2\theta = 5-70^\circ$ . The obtained XRD diffraction patterns were analyzed to calculate the lattice parameters of each sample using the Rietveld Refinement method with Rietica Version 4.2 software. Chemical functional group analysis was conducted using a Thermo Scientific iD1 FTIR spectrometer with KBr pellets. Spectra were collected using 64 scans in the 400–4000 cm<sup>-1</sup> range at a resolution of 4 cm<sup>-1</sup>. Chemical and molecular structures of the samples were analyzed using a Bruker SENTERRA II Raman Microscope with a 785 nm excitation laser, a power output of 10 mW, an aperture of 50 × 1000  $\mu\text{m}$ , a resolution of 4

$\text{cm}^{-1}$ , a spectral range of 45–3630  $\text{cm}^{-1}$ , and a 50 $\times$  magnification microscope. Morphological analysis and elemental distribution on the sample surfaces were observed using a Hitachi SU3500 SEM instrument equipped with an EDS detector. Observations were conducted at an accelerating voltage of 10 kV in secondary electron imaging (SEI) mode with various magnifications. The textural and microporous properties of ZIF-67 and its composites were determined by  $\text{N}_2$  adsorption-desorption at 77 K over a relative pressure range of 0.01–0.99 using a Brunauer-Emmett-Teller (BET) surface area analyzer (BELSOPR MAX G, Japan).

### 3. Results and Discussion

#### 3.1. Characterization of materials.

Metal-organic frameworks (MOFs) ZIF-67 and ZIF-67@ $\text{SiO}_2$  composites were successfully synthesized using the solvothermal method. Figure 1(i) shows the XRD pattern of ZIF-67, exhibiting peaks at  $2\theta = 7.32^\circ$  (001),  $10.35^\circ$  (002),  $12.70^\circ$  (112),  $18.05^\circ$  (222),  $24.35^\circ$  (233), and  $26.57^\circ$  (134). These peaks corresponded to the standard pattern of ZIF-67 (CCDC Code = GITTOT) and aligned with previous studies [53], [56–57].

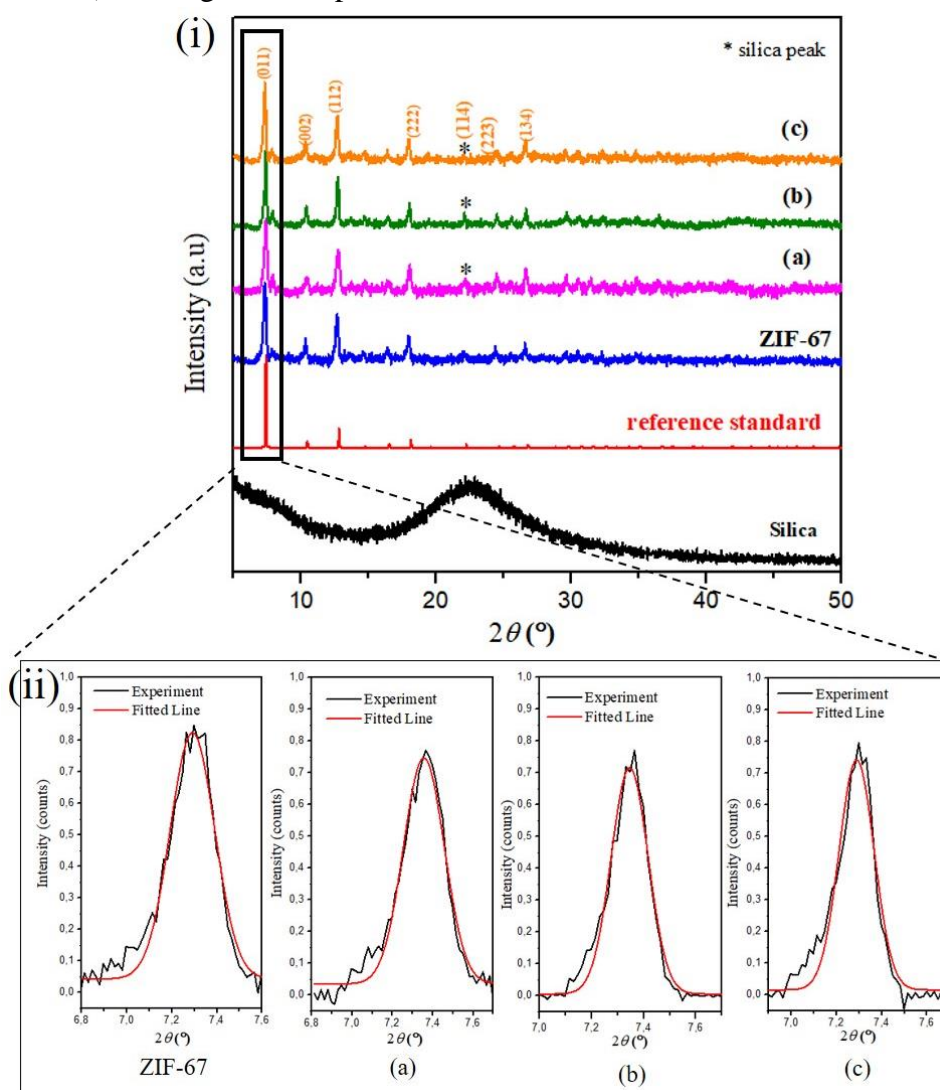


**Figure 1.** (i) XRD pattern of silica, ZIF-67, reference standard (CCDC code = GITTOT), and ZIF-67@ $\text{SiO}_2$  composites with silica variation in (a) 4 %, (b) 8%, and (b) 12%; (ii) fitting on (011) plane of ZIF-67 peak.



The XRD spectrum of the ZIF-67@SiO<sub>2</sub> composite displayed a very similar diffraction pattern to that ZIF-67. Figure 1(i) also indicates that ZIF-67 and ZIF-67@SiO<sub>2</sub> composites exhibited high crystallinity, with the crystallinity degree of ZIF-67 reaching 96.3%. The addition of silica slightly reduced the peak intensity and crystallinity degree, as shown in Figure 1(ii), based on XRD peak fitting at 7.32° (001). Moreover, the degree of crystallinity in the ZIF-67@SiO<sub>2</sub> composite decreased with various silica mass additions but without disrupting the ZIF-67 crystal structure, as presented in Table 1.

**Table 1.** Cell parameters ZIF-67 and ZIF-67@SiO<sub>2</sub>.

Materials	Crystal lattice (Å)	Corner (°)	Cell volume	Rp	Rwp	Degree of crystallinity (%)	Crystal size (nm)
	a=b=c	$\alpha=\beta=\gamma$					
ZIF-67	16.1343 (3)	90	4200.028	1.58	3.59	96,29	10,99
ZIF-67@SiO <sub>2</sub> (4)	16.4384 (2)	90	4442.081	1.76	3.73	90,32	15,46
ZIF-67@SiO <sub>2</sub> (8)	16.4733 (3)	90	4470.421	2.15	3.83	89,45	12,46
ZIF-67@SiO <sub>2</sub> (12)	16.7872 (1)	90	4730.803	2.77	4.02	93,5	13,16

This reduction in peak intensity and crystallinity degree might be attributed to the amorphous nature of the added mesoporous silica [58]. Interestingly, a slight increase in peak intensity at 22–23° was observed, likely due to the overlap of the ZIF-67 peak at 22.09° with the silica peak at  $2\theta = 22.53^\circ$ . The weak representative silica peak might stem from the amorphous nature and low mass percentage of silica. These findings confirmed the successful formation of the ZIF-67@SiO<sub>2</sub> composite material. Table 1 provides the refinement results of the XRD diffraction patterns for each sample, showing cubic crystal symmetry with the space group *I43m* and unit cell parameters  $a = b = c$ . An increase in the percentage of silica mass in ZIF-67 led to larger unit cell parameters and cell volumes without compromising the ZIF-67 crystal structure (see Table 1). This result suggested the incorporation of silica into the ZIF-67 framework. The addition of larger silica particles (mesoporous) compared to ZIF-67 (microporous) likely caused lattice parameters and cell volume expansion [59].

The successful synthesis of ZIF-67 and ZIF-67@SiO<sub>2</sub> composites was further confirmed through FTIR spectroscopy, as shown in Figure 2. The observed peaks were primarily associated with ZIF-67 and were largely due to the organic ligand 2-methylimidazole (2-MeIM). The absorption peak at 419 cm<sup>-1</sup> corresponded to the stretching vibration of Co-N, indicating an interaction between the Co metal and the nitrogen atom of 2-MeIM [60]. The in-plane and out-of-plane bending vibrations, along with the stretching vibration of C=N in the ligand 2-MeIM, appeared at 689 cm<sup>-1</sup>, 755 cm<sup>-1</sup>, and 1578 cm<sup>-1</sup>, respectively. The absorption bands at 993 cm<sup>-1</sup> and 1141 cm<sup>-1</sup> were attributed to the bending and stretching vibrations of C-N. Additionally, the peak at 2921 cm<sup>-1</sup> resulted from the stretching vibration of the aromatic C-H ring in 2-methylimidazole [61] or the symmetric stretching vibration of CH<sub>3</sub> [62]. A broad peak in the 3200–3500 cm<sup>-1</sup> range suggested the presence of bound water in the sample. Silica absorption peaks were detected at 470 cm<sup>-1</sup> and 1109 cm<sup>-1</sup>, corresponding to the bending and asymmetric stretching vibrations of Si-O-Si. In the FTIR spectrum, the increased intensity was evident in the 1109–1141 cm<sup>-1</sup> region, correlating with the vibration peak of SiO<sub>2</sub> molecules. This observation further supported the successful formation of the ZIF-67@SiO<sub>2</sub> composite while maintaining the structural integrity of the ZIF-67 [63].

Raman spectroscopy was utilized to analyze ZIF-67 in greater depth. As shown in Figure 3, the Raman spectrum of ZIF-67 and ZIF-67@SiO<sub>2</sub> composites revealed characteristic peaks of ZIF-67 at 178, 260, and 686 cm<sup>-1</sup>, corresponding to Co ions and 2-methylimidazole ligands of ZIF-67 [54, 64–65].

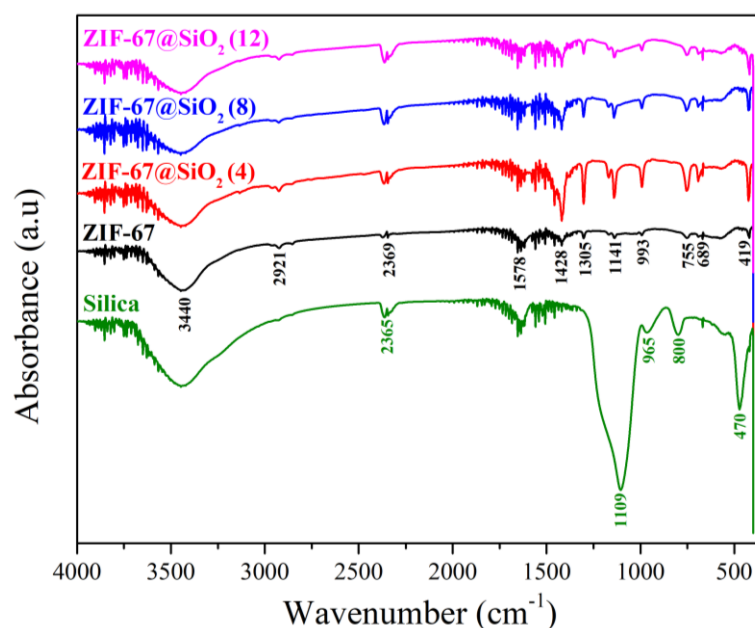


**Figure 2.** FTIR spectra of silica, ZIF-67, and ZIF-67@SiO<sub>2</sub> with different silica concentrations (4, 8, and 12%).

The Raman spectrum also displayed variations in peak intensity and sharpness during the formation of the ZIF-67@SiO<sub>2</sub> composite. Notably, the peak at 686 cm<sup>-1</sup> showed increased intensity with the addition of 4% and 8% silica but slightly decreased when 12% silica was added. The incorporation of silica mesopores into the ZIF-67 structure caused the crystal structure to become denser and the crystal size to increase, as shown in Table 1 [66]. This structural densification explained the initial increase in peak intensity with 4% and 8% silica. However, as more silica was added, the amorphous properties dominated, leading to decreased crystallinity and intensity. These observations were consistent with the XRD characterization results, showing a decline in crystallinity with increasing silica content.

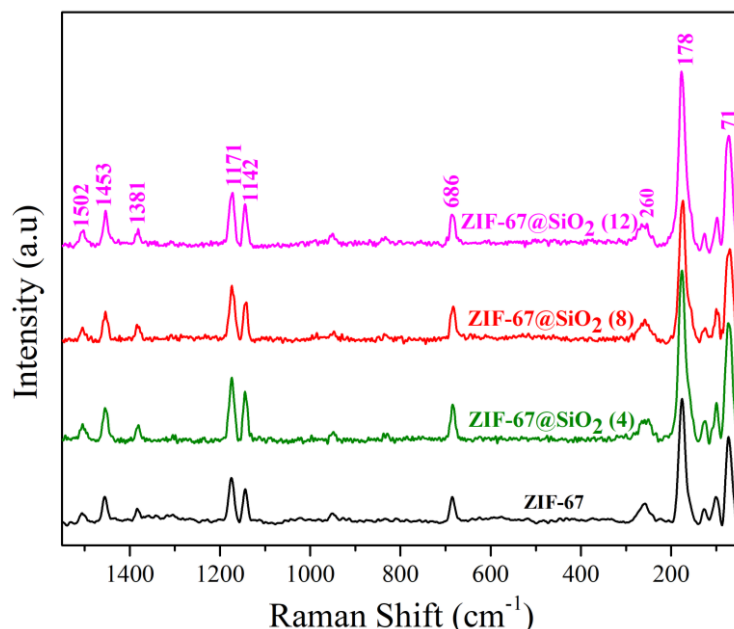


**Figure 3.** Raman spectra of ZIF-67 and ZIF-67@SiO<sub>2</sub> with different silica concentrations (4, 8, and 12%).

Figure 4(i) illustrates the morphology of ZIF-67 and ZIF-67@SiO<sub>2</sub> composites at various silica mass percentages. Both ZIF-67 and ZIF-67@SiO<sub>2</sub> composites exhibited a rhombic dodecahedral particle shape, which is characteristic of ZIF-67 particles [67,68].

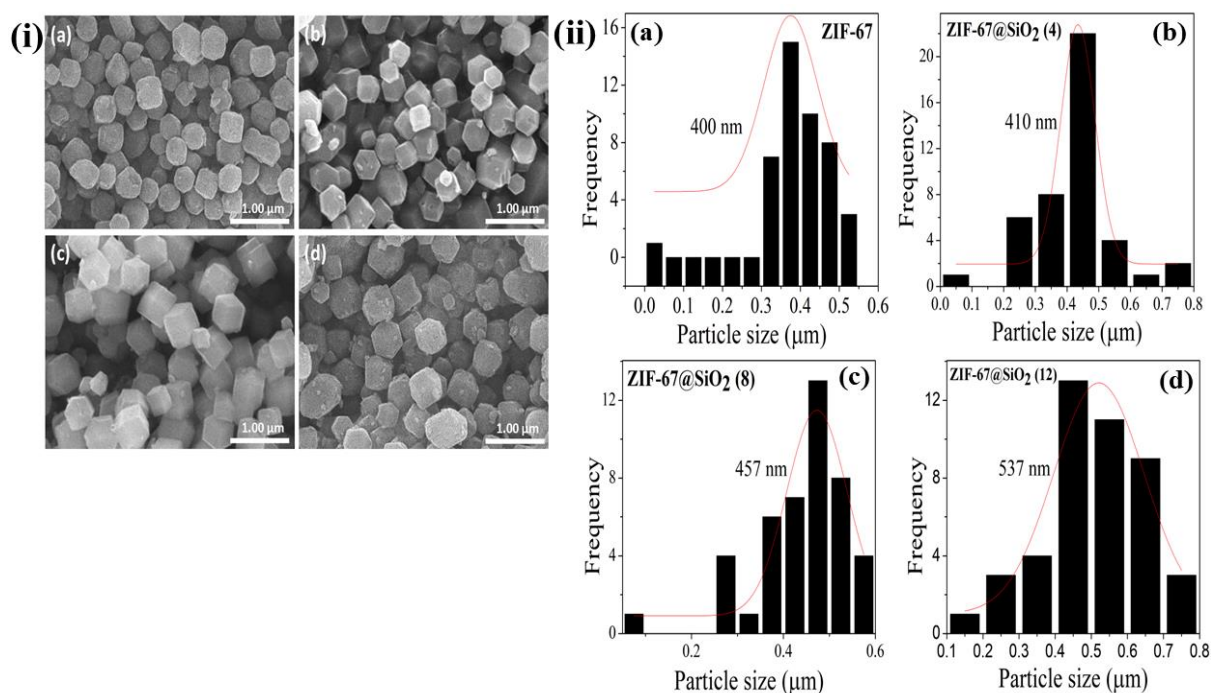


**Figure 4.** (i) SEM micrograph of (a) ZIF-67, (b) ZIF-67@SiO<sub>2</sub> (4%), (c) ZIF-67@SiO<sub>2</sub> (8%), and (d) ZIF-67@SiO<sub>2</sub> (12%); (ii) Histogram of the particle size distribution of samples.

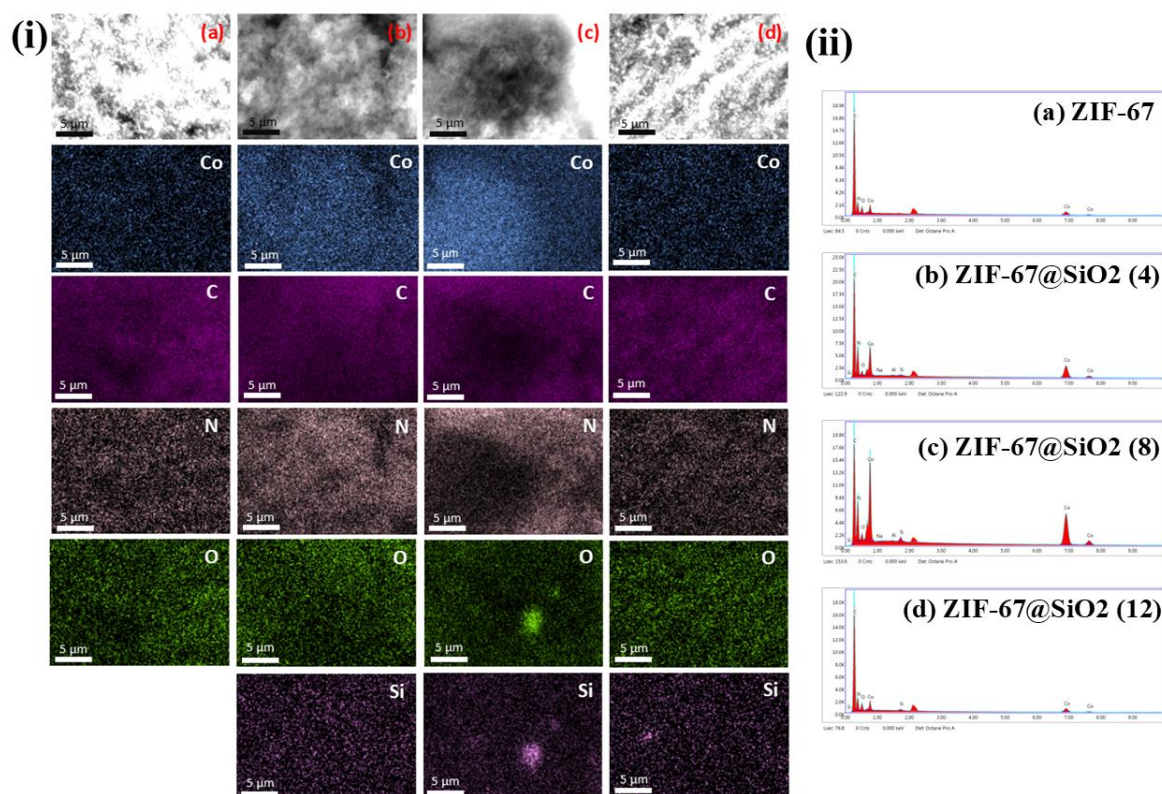


**Figure 5.** (i) Elemental mapping and (ii) EDS spectrum of (a) ZIF-67, (b) ZIF-67@SiO<sub>2</sub> (4), (c) ZIF-67@SiO<sub>2</sub> (8), and (d) ZIF-67@SiO<sub>2</sub> (12).

The addition of silica enhanced the formation of rhombic dodecahedral morphology, as indicated by sharper edges, smoother surfaces, and larger particle sizes (see Fig. S1). However, small silica particles were observed to adhere to the surface of ZIF-67 particles. When 12% silica was added, the crystal structure of ZIF-67 exhibited a reduced crystallinity, increased



crystal size, and a rougher surface texture (see Figure 4d(i)). This decrease in crystallinity with 12% silica addition aligned with the findings from XRD, FTIR, and Raman characterization.

Elemental mapping and distribution of elements in ZIF-67 and ZIF-67@SiO<sub>2</sub> composites are presented in Figure 5. EDS mapping confirmed that Co, C, N, and O were evenly distributed on the material's surface. Co, C, and N were core components of ZIF-67, based on its molecular formula Co(CH<sub>3</sub>C<sub>3</sub>H<sub>3</sub>N<sub>2</sub>)<sub>2</sub>. The element O was introduced by water molecules incorporated into the structure during synthesis [69]. Additionally, a uniform distribution of Si was observed on the surface of ZIF-67@SiO<sub>2</sub> composite particles (see Figure 5b-d), indicating the successful impregnation of silica into ZIF-67 particles. This was further supported by the increasing concentration of silica corresponding to the higher percentage of added silica mass. Detailed information on the elemental content of the materials is provided in Supplementary Table S1.

### 3.2. Adsorption performance.

The nitrogen adsorption-desorption isotherms of ZIF-67 and ZIF-67@SiO<sub>2</sub> at 77 K are shown in Figure 6, and their textural parameters are detailed in Table 2. Based on Figure 6, the physisorption isotherms of ZIF-67 and ZIF-67@SiO<sub>2</sub> were classified as type I microstructure isotherms, according to IUPAC [70]. The isotherms showed a sharp increase in adsorption at low relative pressure ( $P/P_0$  below 0.1), characteristic of microporous materials. For ZIF-67@SiO<sub>2</sub>, the amount of adsorbed gas increased, and a narrow vertical hysteresis loop indicated capillary condensation in mesopores [54], [71-72].

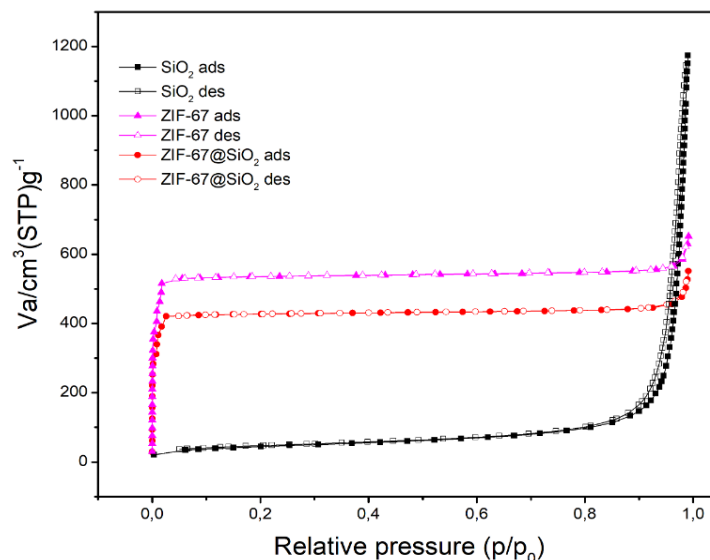


**Figure 6.** N<sub>2</sub> adsorption-desorption isotherms.

**Table 2.** Textural parameters of the samples.

Samples	S <sub>BET</sub> (m <sup>2</sup> /g)	Volume total (cm <sup>3</sup> /g)	Average pore size (nm)
Silica	153.73	1.7971	23.379
ZIF-67	2077	0.9807	0.9443
ZIF-67@SiO <sub>2</sub> (8)	1626	0.8215	1.0104

The pore size distribution, determined using the nonlocal density functional theory (NLDFT) method, is displayed in Figure 7. The maximum pore size distribution curve for ZIF-67 and ZIF-67@SiO<sub>2</sub> was observed at 1.6 nm and 1.7 nm, respectively, indicating that both samples possessed micropores. The specific surface area (SSA) of ZIF-67 and ZIF-67@SiO<sub>2</sub>

was calculated using the BET model, yielding values of 2077 m<sup>2</sup>/g and 1626 m<sup>2</sup>/g, respectively. The BET SSA of ZIF-67 in this study was higher than previously reported values by Nazir *et al.* [73] (1030 m<sup>2</sup>/g), Wang *et al.* [74] (1780 m<sup>2</sup>/g), and Saghir and Xiao [68] (1138.65 m<sup>2</sup>/g), suggesting that the synthesis method used here produced ZIF-67 with a larger specific surface area. The SSA of ZIF-67@SiO<sub>2</sub> was smaller than that of ZIF-67, highlighting the contribution of silica. Silica could block some of the pores in ZIF-67, resulting in a reduced SSA for the composite. The addition of silica to ZIF-67 has been reported to either decrease [54] or increase [38] the surface area, depending on the synthesis conditions. Furthermore, the pore volume of ZIF-67 decreased from 0.9807 cm<sup>3</sup>/g to 0.8215 cm<sup>3</sup>/g upon the addition of silica in ZIF-67@SiO<sub>2</sub>. However, the pore size of ZIF-67@SiO<sub>2</sub> was larger than that of ZIF-67 alone. These findings were consistent with studies by Lei *et al.* [75] and Saghir and Xiao [68], reporting that the incorporation of Fe<sub>3</sub>O<sub>4</sub> or Ag particles into ZIF-67 reduced its specific surface area. The observed decrease in specific surface area, pore volume, and active sites in ZIF-67@SiO<sub>2</sub> could be attributed to the dilution effect caused by mesoporous silica [76]. The results of the N<sub>2</sub> adsorption-desorption analysis indicated that ZIF-67 possessed a large specific surface area, providing more active sites and a larger contact area, which was advantageous for adsorption applications [77].

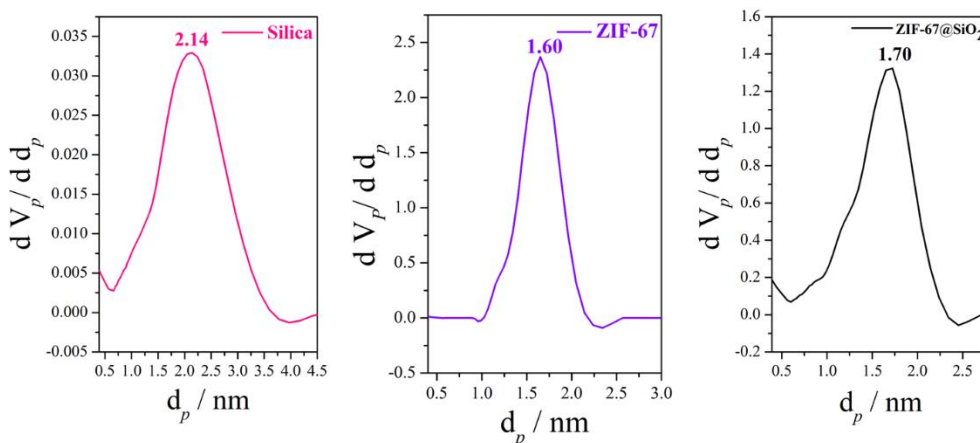


**Figure 7.** Pore size distribution with NLDFT model.

### 3.3. Photodegradation of CGR in ZIF-67 and ZIF-67@SiO<sub>2</sub> under sunlight.

The reaction mixture was maintained in a dark environment for 30 minutes to achieve adsorption-desorption equilibrium before the photocatalytic activity test. For the photocatalytic activity test, the saturated dye concentration was used as the initial dye concentration (C<sub>0</sub>). The photodegradation performance of ZIF-67 and ZIF-67@SiO<sub>2</sub> toward Congo red (CGR) under sunlight exposure for contact times ranging from 30 to 120 minutes is shown in Figure 8.

ZIF-67 exhibited the highest photodegradation efficiency toward CGR, achieving 85.32% degradation with an adsorption capacity of 67.66 mg/g at a contact time of 120 minutes. The relatively large specific surface area, pore volume, and pore size of ZIF-67 facilitated the diffusion of CGR dye molecules onto its surface, where they interacted electrostatically with cobalt ions [68, 78]. Furthermore, the positive surface charge of ZIF-67 (zeta potential values ranging from 2.88 mV to 14.37 mV at pH 7–10) enhanced its effectiveness in degrading anionic dyes such as CGR [20, 28]. The effect of contact time on photodegradation activity was evaluated using a one-way analysis of variance (ANOVA) at a significance level of  $\alpha = 0.05$  in Microsoft Excel. The results revealed that contact time significantly affected the degradation

activity (% degradation) of CGR, with a p-value of 0.0029 ( $p < 0.05$ ) (data presented in Table S2) [79].

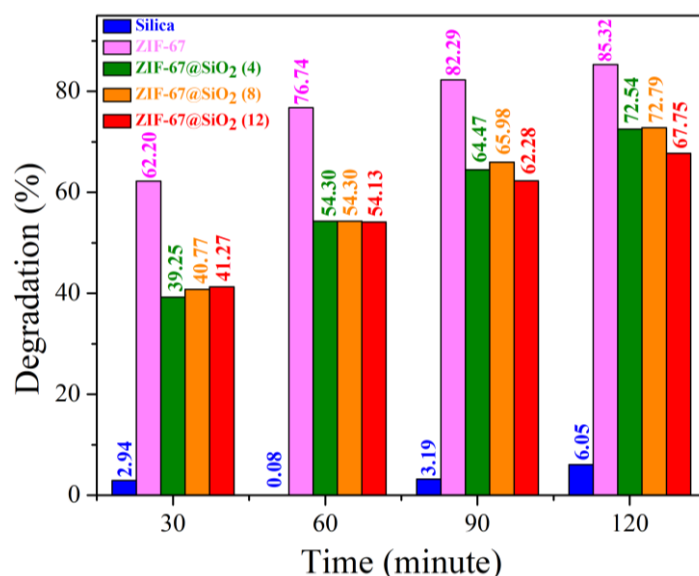


**Figure 8.** Congo red degradation of ZIF-67 and ZIF-67@SiO<sub>2</sub>.

The addition of silica to ZIF-67 resulted in a 12.5% reduction in degradation efficiency toward CGR, attributed to textural changes such as a decrease in pore volume and specific surface area. However, when 8% silica was added, ZIF-67@SiO<sub>2</sub> achieved a maximum degradation percentage of 72.79% with an adsorption capacity of 57.7 mg/g at a contact time of 120 minutes. The composite's capacity to degrade CGR exhibits a higher degradation percentage than prior studies by Guan *et al.*, which demonstrated that the Fe<sub>3</sub>O<sub>4</sub>@ZIF-67 composite was capable of decomposing Congo red by 70% [80]. In contrast, research by Tong *et al.* indicated that ZIF-67@CeO could achieve a more optimal degradation of Congo red, reaching 98.8%, though with the inclusion of a persulfate activator [81]. Murali *et al.* conducted degradation studies of ZIF-67 on methylene blue, confirming its capacity to efficiently degrade up to 80% within 180 minutes [82]. The adsorption capacity ( $Q_t$ ) of all composite samples increased with a contact time of up to 120 minutes, even though the degradation efficiency of ZIF-67@SiO<sub>2</sub> decreased (see Figure 9). Specifically, the adsorption capacity of ZIF-67, ZIF-67@SiO<sub>2</sub> (4), ZIF-67@SiO<sub>2</sub> (8), and ZIF-67@SiO<sub>2</sub> (12) increased by 5.75%, 8.5%, 8.25%, and 7.23%, respectively, across different contact times, indicating that ZIF-67@SiO<sub>2</sub> had a higher adsorption capacity rate compared to ZIF-67.

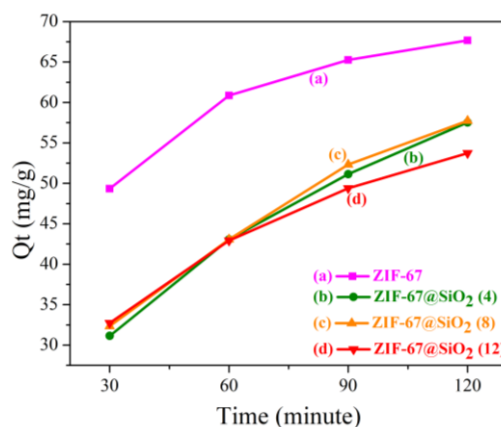


**Figure 9.** Adsorption capacity curve of Congo red.

The reaction rate for each sample was determined using adsorption kinetics models, specifically the pseudo-first-order (PFO) and pseudo-second-order (PSO) equations as follows:

$$\ln(Q_e - Q_t) = \ln Q_e - K_1 t \quad (3)$$

$$\frac{t}{Q_t} = \frac{1}{K_2 Q_e^2} + \frac{t}{Q_e} \quad (4)$$

The PFO and PSO kinetic models for CGR adsorption in this study are shown in Figures 10a and 10b. The adsorption kinetics were evaluated by comparing the  $R^2$  values of each model, as detailed in Table 3. The PFO model predicted adsorption kinetics by plotting  $\ln(Q_e - Q_t)$  versus  $t$ , resulting in a straight line with a negative slope  $K_1$  and intercept  $\ln Q_e$ . Similarly, the PSO model was evaluated by plotting  $t/Q_t$  versus  $t$ . The results indicated that the  $R^2$  value of the PSO model was greater than that of the PFO model, suggesting that the adsorption process of CGR by ZIF-67 and ZIF-67@SiO<sub>2</sub> followed the pseudo-second-order kinetics model. This result implied that the adsorption process was chemically driven (chemisorption) and involved electrostatic interactions between the catalyst and CGR [49].

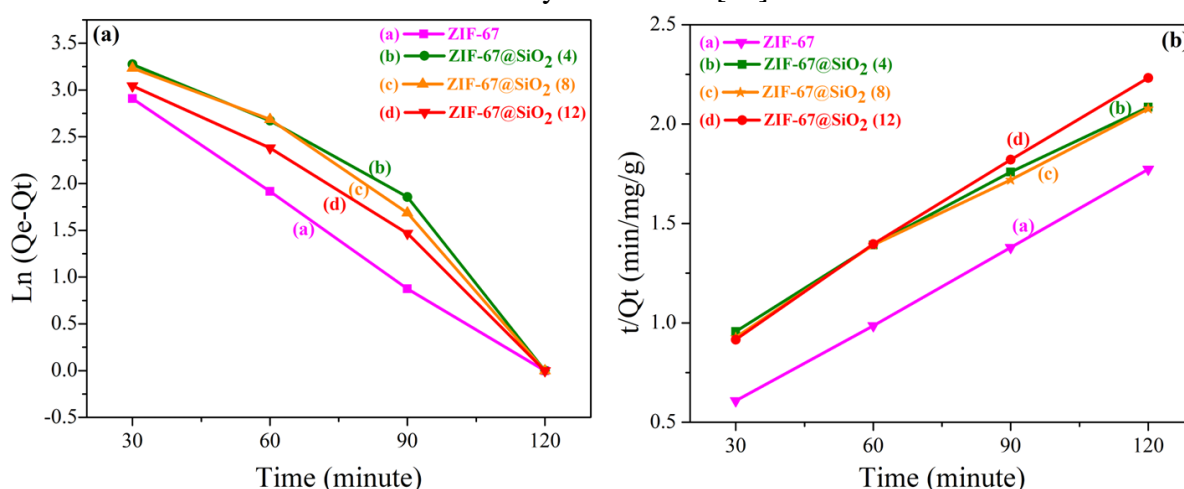


**Figure 10.** Plots of (a) pseudo-first-order; (b) pseudo-second-order kinetics for the adsorption of CGR.

**Table 3.** Kinetic parameters and correlation coefficients for the pseudo-first-order and pseudo-second-order equations.

Catalyst	$Q_{e(\text{exp})}$	Pseudo-first-order			Pseudo-second-order		
		$Q_{e(\text{cal})}$	$K_1$	$R^2$	$Q_{e(\text{cal})}$	$K_2$	$R^2$
ZIF-67	67.6666	51.0697	0.0339	0.9937	76.9230	27.616	0.9999
ZIF-67@SiO <sub>2</sub> (4)	57.5333	55.5444	0.0236	0.9925	80.6451	10.536	0.9961
ZIF-67@SiO <sub>2</sub> (8)	57.7333	59.3514	0.0258	0.9726	79.3650	10.764	0.994
ZIF-67@SiO <sub>2</sub> (12)	53.7333	48.1633	0.0263	0.9918	68.4931	9.416	0.9986

The correlation between the degree of crystallinity and specific surface area (SSA) on the degradation performance of the samples against Congo red is summarized in Table 4.

**Table 4.** The correlation between the degree of crystallinity, specific surface area (SSA), and degradation performance of samples.

Samples	Degree of crystallinity (%)	Specific surface area (m <sup>2</sup> /g)	Congo red degradation (%)	Adsorption capacity rate (%)
Silica	Amorphous	153.73	6.05	3.06
ZIF-67	96.29	2077	85.32	5.75
ZIF-67@SiO <sub>2</sub> (8)	89.45	1626	72.79	8.25

The mechanism of CGR degradation using the ZIF-67@SiO<sub>2</sub> catalyst involved the formation of reactive oxygen species. When exposed to sunlight, electrons in the valence band



were excited to the conduction band, generating electron-hole pairs ( $e^-$  and  $h^+$ ). These electrons and holes reacted with oxygen and water to form superoxide radicals ( $O_2^{\cdot-}$ ) and hydroxyl radicals ( $\cdot OH$ ), which were highly reactive. These reactive species degraded CGR dye into harmless products such as  $H_2O$  and  $CO_2$ . Overall, ZIF-67@ $SiO_2$  effectively enhanced the photodegradation of pollutants through the generation of reactive oxygen species [83]. An illustration of the photodegradation mechanism of Congo red from ZIF-67@ $SiO_2$  in this study is shown in Figure 11.

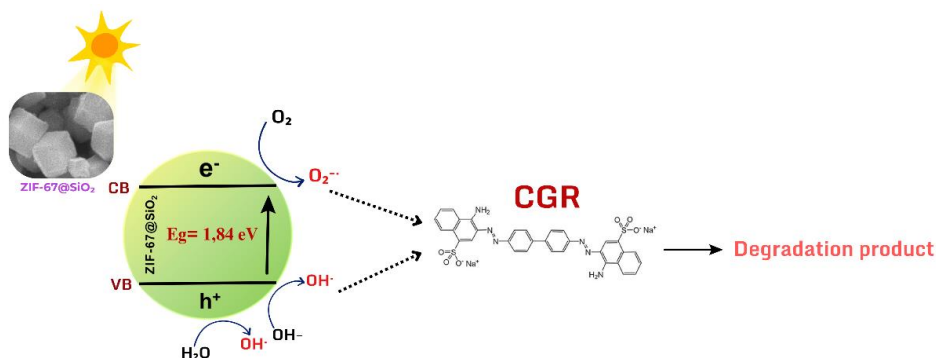


**Figure 11.** The Illustration of the photodegradation mechanism of Congo red from ZIF-67@ $SiO_2$ .

#### 4. Conclusion

ZIF-67 and silica-based ZIF-67 (ZIF-67@ $SiO_2$ ) composites were successfully synthesized using a solvothermal method with methanol as the solvent. XRD, FTIR, and Raman spectroscopy analyses confirmed that the addition of silica to ZIF-67 resulted in the formation of the ZIF-67 composite without altering its crystal structure. SEM analysis indicated that increasing the silica percentage effectively improved the rhombic dodecahedron crystal morphology and increased crystal size but reduced crystallinity. Elemental mapping confirmed the successful impregnation of silica, exhibiting the presence of Co, C, N, O, and Si on the surface of ZIF-67@ $SiO_2$ . Texture analysis revealed that both ZIF-67 and ZIF-67@ $SiO_2$  were microporous materials, with specific surface areas of 2077  $m^2/g$  and 1626  $m^2/g$ , respectively. The photocatalytic activity tests showed that ZIF-67 and ZIF-67@ $SiO_2$  (8%) effectively degraded Congo red (CGR) under direct sunlight after 120 minutes, achieving 85.32% and 72.79%, respectively. Therefore, this research concludes that ZIF-67@ $SiO_2$  (8%) exhibited the best performance as a catalyst for degrading Congo red dye. Further research is recommended to optimize the photocatalytic performance of the ZIF-67@ $SiO_2$  composite to remove other organic pollutants. ZIF-67-based materials modified with micro, meso, and macroporous materials have great potential in the removal of pollutants in aquatic systems due to pore characteristics that can increase diffusion rates and reduce mass transfer barriers of reactant or product molecules. However, large-scale production of ZIF-67-based materials for photocatalytic applications in industrial wastewater systems must consider the use of synthesis methods through simple, low-cost, and environmentally friendly approaches. This is a challenge and concern for the development of more optimized and efficient ZIF-67 materials in the future.

#### Author Contributions

Conceptualization, E.M.; methodology, E.M.; software, W.A.; validation, E.A., N.K., and G.T.; formal analysis, E.M., N.K., and G.T.; investigation, E.M.; resources, W.A.; data

<https://biointerfaceresearch.com/>

curation, E.A. and K.C.; writing—original draft preparation, E.M.; writing—review and editing, E.M.; visualization, W.A.; project administration, W.A.; funding acquisition, E.M. All authors have read and agreed to the published version of the manuscript.

### **Institutional Review Board Statement**

Not applicable.

### **Data Availability Statement**

The data of this study are available from the corresponding author upon reasonable request.

### **Funding**

This research was supported by a research grant under the Collaboration Scheme with Business, Industry, Research Institutions, and Local Government, Faculty of Mathematics and Natural Sciences, Universitas Bengkulu, Fiscal Year 2024, with the contract number of 2696/UN30.12/HK/2024, dated May 21, 2024.

### **Acknowledgments**

We would like to thank the Office Partnership International Affairs, Universitas Bengkulu, through the Implementation Arrangement to university within QS. 200 Year 2024 program for research collaboration between Bengkulu University and Universiti Malaya.

### **Conflicts of Interest**

The authors declare no conflict of interest.

### **References**

1. Islam, T.; Repon, M.R.; Islam, T.; Sarwar, Z.; Rahman, M.M. Impact of textile dyes on health and ecosystem: a review of structure, causes, and potential solutions. *Environ. Sci. Pollut. Res.* **2023**, *30*, 9207–9242, <https://doi.org/10.1007/s11356-022-24398-3>.
2. Dang, G.H.; Le, T.T.A.; Ta, A.K.; Ho, T.N.T.; Pham, T.V.; Doan, T.V.H.; Luong, T.H.V. Removal of Congo red and malachite green from aqueous solution using heterogeneous Ag/ZnCo-ZIF catalyst in the presence of hydrogen peroxide. *Green Process. Synth.* **2020**, *9*, 567–577, <https://doi.org/10.1515/gps-2020-0060>.
3. Dutta, S.; Adhikary, S.; Bhattacharya, S.; Roy, D.; Chatterjee, S.; Chakraborty, A.; Banerjee, D.; Ganguly, A.; Nanda, S.; Rajak, P. Contamination of textile dyes in aquatic environment: Adverse impacts on aquatic ecosystem and human health, and its management using bioremediation. *J. Environ. Manag.* **2024**, *353*, 120103, <https://doi.org/10.1016/j.jenvman.2024.120103>.
4. Periyasamy, A.P. Recent advances in the remediation of textile-dye-containing wastewater: prioritizing human health and sustainable wastewater treatment. *Sustainability* **2024**, *16*, 495 5, <https://doi.org/10.3390/su16020495>.
5. Khan, R.R.M.; Qamar, H.; Hameed, A.; Rehman, A.u.; Pervaiz, M.; Saeed, Z.; Adnan, A.; Ch, A.R. Biological and photocatalytic degradation of congo red, a diazo sulfonated substituted dye: a Review. *Water Air Soil Pollut.* **2022**, *233*, 468, <https://doi.org/10.1007/s11270-022-05935-9>.
6. Kumaravel, R.; Shanmugam, V.K. Biomimetic and ecological perspective towards decolorization of industrial important azo dyes using bacterial cultures – A review. *Sustain. Chem. Environ.* **2024**, *7*, 100130, <https://doi.org/10.1016/j.scenv.2024.100130>.

7. Kusumlata; Ambade, B.; Kumar, A.; Gautam, S. Sustainable solutions: reviewing the future of textile dye contaminant removal with emerging biological treatments. *Limnol. Rev.* **2024**, *24*, 126-149, <https://doi.org/10.3390/limnolrev24020007>.
8. Sarker, T.; Tahmid, I.; Sarker, R.K.; Dey, S.C.; Islam, M.T.; Sarker, M. ZIF-67-based materials as adsorbent for liquid phase adsorption-a review. *Polyhedron* **2024**, *260*, 117069, <https://doi.org/10.1016/j.poly.2024.117069>.
9. Das, T.; Debnath, A.; Manna, M.S. Adsorption of malachite green by aegle marmelos-derived activated biochar: Novelty assessment through phytotoxicity tests and economic analysis. *J. Indian Chem. Soc.* **2024**, *101*, 101219, <https://doi.org/10.1016/j.jics.2024.101219>.
10. Ledakowicz, S.; Paździor, K. Recent achievements in dyes removal focused on advanced oxidation processes integrated with biological methods. *Molecules* **2021**, *26*, 870, <https://doi.org/10.3390/molecules26040870>.
11. Ahmadi, S.A.R.; Kalaei, M.R.; Moradi, O.; Nosratinia, F.; Abdouss, M. Synthesis of novel zeolitic imidazolate framework (ZIF-67) – zinc oxide (ZnO) nanocomposite (ZnO@ZIF-67) and potential adsorption of pharmaceutical (tetracycline (TCC)) from water. *J. Mol. Struct.* **2022**, *1251*, 132013, <https://doi.org/10.1016/j.molstruc.2021.132013>.
12. Adawiah, A.; Gunawan, M.S.; Aziz, I.; Oktavia, W. Synthesis of bimetallic metal-organic frameworks (MOFs) La-Y-PTC for enhanced dyes photocatalytic degradation. *Bull. Chem. React. Eng. Catal.* **2023**, *18*, 118-130, <https://doi.org/10.9767/bcrec.16130>.
13. Bopape, D.A.; Ntsendwana, B.; Mabasa, F.D. Photocatalysis as a pre-discharge treatment to improve the effect of textile dyes on human health: A critical review. *Heliyon* **2024**, *10*, e39316, <https://doi.org/10.1016/j.heliyon.2024.e39316>.
14. Li, X.; Fu, L.; Chen, F.; Zhao, S.; Zhu, J.; Yin, C. Application of heterogeneous catalytic ozonation in wastewater treatment: An overview. *Catalysts* **2023**, *13*, 342, <https://doi.org/10.3390/catal13020342>.
15. Shan, Y.; Zhang, G.; Shi, Y.; Pang, H. Synthesis and catalytic application of defective MOF materials. *Cell Rep. Phys. Sci.* **2023**, *4*, 101301, <https://doi.org/10.1016/j.xcrp.2023.101301>.
16. Behrooz, A.H.; Xu, R. Photocatalytic CO<sub>2</sub> reduction: photocatalysts, membrane reactors, and hybrid processes. *Chem Catalysis* **2023**, *3*, 100550, <https://doi.org/10.1016/j.checat.2023.100550>.
17. Huang, L.; Yang, J.; Zhao, Y.; Miyata, H.; Han, M.; Shuai, Q.; Yamauchi, Y. Monolithic covalent organic frameworks with hierarchical architecture: attractive platform for contaminant remediation. *Chem. Mater.* **2023**, *35*, 2661-2682, <https://doi.org/10.1021/acs.chemmater.2c03282>.
18. Jadhav, H.S.; Bandal, H.A.; Ramakrishna, S.; Kim, H. Critical review, recent updates on zeolitic imidazolate framework-67 (ZIF-67) and its derivatives for electrochemical water splitting. *Adv. Mater.* **2022**, *34*, 2107072, <https://doi.org/10.1002/adma.202107072>.
19. Bhatt, C.S.; Parimi, D.S.; Khan, S.; Dasari, V.V.; Paila, B.; Mishra, A.; Marpu, S.; Suresh, A.K. Sustainable hand-retrievable wide-area supported catalysts for waste water remediation: Role of support features in mitigating the catalytic performance. *Coordination Chemistry Reviews* **2024**, *516*, 215993, <https://doi.org/10.1016/j.ccr.2024.215993>.
20. Zhang, C.; Lin, Z.; Jiao, L.; Jiang, H.-L. Metal-organic frameworks for electrocatalytic CO<sub>2</sub> reduction: from catalytic site design to microenvironment modulation. *Angew. Chem. Int. Ed.* **2024**, *63*, e202414506, <https://doi.org/10.1002/anie.202414506>.
21. Hussain, M.Z.; Yang, Z.; Huang, Z.; Jia, Q.; Zhu, Y.; Xia, Y. Recent advances in metal-organic frameworks derived nanocomposites for photocatalytic applications in energy and environment. *Adv. Sci.* **2021**, *8*, 2100625, <https://doi.org/10.1002/advs.202100625>.
22. Kiteto, M.; Vidija, B.; Mecha, C.A.; Mrosso, R.; Chollom, M.N. Advances in metal-organic frameworks as adsorbents, photocatalysts and membranes: a new frontier in water purification. *Discover Water* **2024**, *4*, 54, <https://doi.org/10.1007/s43832-024-00119-4>.
23. Singh, S.; Sivaram, N.; Nath, B.; Khan, N.A.; Singh, J.; Ramamurthy, P.C. Metal organic frameworks for wastewater treatment, renewable energy and circular economy contributions. *npj Clean Water* **2024**, *7*, 124, <https://doi.org/10.1038/s41545-024-00408-4>.
24. Sabzehmeidani, M.M.; Gafari, S.; Jamali, S.; Kazemzad, M. Concepts, fabrication and applications of MOF thin films in optoelectronics: A review. *Appl. Mater. Today* **2024**, *38*, 102153, <https://doi.org/10.1016/j.apmt.2024.102153>.

25. Tang, S.; Wang, Y.; He, P.; Wang, Y.; Wei, G. Recent advances in metal–organic framework (MOF)-based composites for organic effluent remediation. *Materials* **2024**, *17*, 2660, <https://doi.org/10.3390/ma17112660>.
26. Duan, C.; Yu, Y.; Hu, H. Recent progress on synthesis of ZIF-67-based materials and their application to heterogeneous catalysis. *Green Energy Environ.* **2020**, *7*, 3-15, <https://doi.org/10.1016/j.gee.2020.12.023>.
27. Khan, A.; Sadiq, S.; Khan, I.; Humayun, M.; Jiyuan, G.; Usman, M.; Khan, A.; Khan, S.; Alanazi, A.F.; Bououdina, M. Preparation of visible-light active MOFs-Perovskites (ZIF-67/LaFeO<sub>3</sub>) nanocatalysts for exceptional CO<sub>2</sub> conversion, organic pollutants and antibiotics degradation. *Heliyon* **2024**, *10*, e27378, <https://doi.org/10.1016/j.heliyon.2024.e27378>.
28. Payam, A.F.; Khalil, S.; Chakrabarti, S. Synthesis and characterization of MOF-derived structures: Recent advances and future perspectives. *Small* **2024**, *20*, 2310348. <https://doi.org/10.1002/smll.202310348>.
29. Sağlam, S.; Türk, F.N.; Arslanoğlu, H. Use and applications of metal-organic frameworks (MOF) in dye adsorption: Review. *J. Environ. Chem. Eng.* **2023**, *11*, 110568, <https://doi.org/10.1016/j.jece.2023.110568>.
30. Arya, K.; Kumar, A.; Kataria, R. Recent advances in MOF-based composites for the detection and adsorptive removal of Pb(II) ions in aqueous phase. *Mater. Today Sustain.* **2025**, *29*, 101057, <https://doi.org/10.1016/j.mtsust.2024.101057>.
31. Pouramini, Z.; Mousavi, S.M.; Babapoor, A.; Hashemi, S.A.; Lai, C.W.; Mazaheri, Y.; Chiang, W.-H. Effect of metal atom in zeolitic imidazolate frameworks (ZIF-8 & 67) for removal of dyes and antibiotics from wastewater: a review. *Catalysts* **2023**, *13*, 155, <https://doi.org/10.3390/catal13010155>.
32. Nazir, M.A.; Ullah, S.; Shahid, M.U.; Hossain, I.; Najam, T.; Ismail, M.A.; Rehman, A.u.; Karim, M.R.; Shah, S.S.A. Zeolitic imidazolate frameworks (ZIF-8 & ZIF-67): Synthesis and application for wastewater treatment. *Sep. Purif. Technol.* **2025**, *356*, 129828, <https://doi.org/10.1016/j.seppur.2024.129828>.
33. Younis, S.A.; Kwon, E.E.; Qasim, M.; Kim, K.-H.; Kim, T.; Kukkar, D.; Dou, X.; Ali, I. Metal-organic framework as a photocatalyst: Progress in modulation strategies and environmental/energy applications. *Prog. Energy Combust.* **2020**, *81*, 100870, <https://doi.org/10.1016/j.pecs.2020.100870>.
34. Chen, G.; Guan, M.; Yang, Z.; Mi, F.; Wang, Y.; Rao, X. High adsorption separation capacity magnetic MOF-based substrate Fe<sub>3</sub>O<sub>4</sub>@ZIF-67@Ag for sensitive and recyclable SERS detection of malachite green in aquaculture. *Microchem. J.* **2024**, *207*, 112098, <https://doi.org/10.1016/j.microc.2024.112098>.
35. Hu, Y.; Li, W.; Wei, Z.; Yang, H.; Wang, Y.; Li, S. Advances in electrochemical sensing with ZIF-67 and related materials. *Int. J. Electrochem. Sci.* **2023**, *18*, 100180, <https://doi.org/10.1016/j.ijoes.2023.100180>.
36. Kumar, D.; Joshi, A.; Singh, G.; Sharma, R.K. Polyoxometalate/ZIF-67 composite with exposed active sites as aqueous supercapacitor electrode. *Chem. Eng. J.* **2022**, *431*, 134085, <https://doi.org/10.1016/j.cej.2021.134085>.
37. Guo, X.; Kang, C.; Huang, H.; Chang, Y.; Zhong, C. Exploration of functional MOFs for efficient removal of fluoroquinolone antibiotics from water. *Microporous Mesoporous Mater.* **2019**, *286*, 84-91, <https://doi.org/10.1016/j.micromeso.2019.05.025>.
38. Chen, Y.; Li, X.; Zhang, J.; Zhao, N.; Dai, L.; Jiang, X.; Liu, C.; Lyu, S.; Li, Z. Preparation of SiO<sub>2</sub> immobilized Co-based catalysts from ZIF-67 and the enhancement effect for Fischer-Tropsch synthesis. *Appl. Catal. B: Environ.* **2021**, *289*, 120027, <https://doi.org/10.1016/j.apcatb.2021.120027>.
39. Nakkhong, T.; Inprasit, T.; Pangon, A. Zeolite imidazole framework-67 (ZIF-67)/phosphorus-doped carbon nanofiber hybrid materials for binder-free supercapacitor electrodes. *Chem. Eng. J.* **2024**, *497*, 154655, <https://doi.org/10.1016/j.cej.2024.154655>.
40. Xuan, K.; Wang, J.; Gong, Z.; Wang, X.; Li, J.; Guo, Y.; Sun, Z. Hydroxyapatite modified ZIF-67 composite with abundant binding groups for the highly efficient and selective elimination of uranium (VI) from wastewater. *J. Hazard. Mater.* **2022**, *426*, 127834, <https://doi.org/10.1016/j.jhazmat.2021.127834>.
41. Supritha, K.M.; Suma, B.P.; Pandurangappa, M. Fabrication of ZIF-67/CNF/PANI composite for selective and sensitive determination of dopamine. *J. Appl. Electrochem.* **2023**, *53*, 2457-2468, <https://doi.org/10.1007/s10800-023-01925-9>.
42. Yeerken, A.; Lin, J.; Wang, X.; Luo, Y.; Ma, H. Fabrication of novel porous ZIF-67/PES composite microspheres and the efficient adsorption of triphenylmethane dyes from water. *CrystEngComm* **2023**, *25*, 1076-1089, <https://doi.org/10.1039/D2CE01486F>.
43. Singh, S.; N, P.; Uppara, B.; Varshney, R.; Shehata, N.; Khan, N.A.; Joji, J.; Singh, J.; Ramamurthy, P.C. Facile Synthesis of ZIF-67-incorporated electrospun PVA nanofibers composite for efficient Pb (II)



- adsorption from water: docking and experimental studies. *ACS EST Water* **2024**, *4*, 4497-4509, <https://doi.org/10.1021/acsestwater.4c00500>.
44. Boonphan, S.; Prachakiew, S.; Klinbumrung, K.; Thongrote, C.; Klinbumrung, A. Enhancing photocatalytic performance of kaolin clay: an overview of treatment strategies and applications. *Arch. Environ. Prot.* **2024**, *50*, 54-64, <https://doi.org/10.24425/aep.2024.151686>.
  45. Wang, F.; Fu, H.; Wang, F.-X.; Zhang, X.-W.; Wang, P.; Zhao, C.; Wang, C.-C. Enhanced catalytic sulfamethoxazole degradation via peroxymonosulfate activation over amorphous CoSx@SiO<sub>2</sub> nanocages derived from ZIF-67. *J. Hazard. Mater.* **2022**, *423*, 126998, <https://doi.org/10.1016/j.jhazmat.2021.126998>.
  46. Li, R.; Wen, X.; Zhao, Y.; Fan, S.; Wei, Q.; Lan, K. Metal-based mesoporous frameworks as high-performance platforms in energy storage and conversion. *Energy Rev.* **2025**, *4*, 100108, <https://doi.org/10.1016/j.enrev.2024.100108>.
  47. Pawar, R.R.; Chuaicham, C.; Sekar, K.; Rajendran, S.; Sasaki, K. Synthesis, characterization, and application of MOF@clay composite as a visible light-driven photocatalyst for rhodamine B degradation. *Chemosphere* **2022**, *291*, 132922, <https://doi.org/10.1016/j.chemosphere.2021.132922>.
  48. Far, H.S.; Najafi, M.; Hasanzadeh, M.; Rahimi, R. A 3D-printed hierarchical porous architecture of MOF@clay composite for rapid and highly efficient dye scavenging. *New J. Chem.* **2022**, *46*, 23351-23360, <https://doi.org/10.1039/D2NJ05188E>.
  49. Salsabila, R.A.; Ediati, R.; Fansuri, H.; Burhan, R.Y.P. Fabrication of bentonite/ZIF-8 composites for photocatalytic removal of congo red in water. *Case Stud. Chem. Environ. Eng.* **2024**, *10*, 100985, <https://doi.org/10.1016/j.csee.2024.100985>.
  50. Sun, H.; Ju, C.; Zhao, Y.; Wang, C.; Peng, X.; Wu, Y. Preparation of SiO<sub>2</sub>@ZIF-67/CNTs and research on its adsorption performance at low-temperature. *Colloids Surf. A: Physicochem. Eng. Asp.* **2020**, *603*, 125205, <https://doi.org/10.1016/j.colsurfa.2020.125205>.
  51. Wang, Q.; Yu, Z.; Zhu, X.; Xiang, Q.; Chen, H.; Pang, Y. ZIF-67 modified MXene/sepiolite composite membrane for oil-water separation and heavy metal removal. *J. Ind. Eng. Chem.* **2022**, *115*, 314-328, <https://doi.org/10.1016/j.jiec.2022.08.014>.
  52. Bigdeloo, M.; Ehsani, A.; Asgari, E.; Alamgholiloo, H. Designing of SiO<sub>2</sub> immobilized Co-based from ZIF-67 for high-performance supercapacitors. *Inorg. Chem. Commun.* **2024**, *170*, 113321, <https://doi.org/10.1016/j.inoche.2024.113321>.
  53. Saeed, S.; Bashir, R.; Rehman, S.U.; Nazir, M.T.; Alothman, Z.A.; Muteb Aljuwayid, A.; Abid, A.; Adnan, A. Synthesis and characterization of ZIF-67 mixed matrix nanobiocatalysis for CO<sub>2</sub> adsorption performance. *Front. Bioeng. Biotechnol.* **2022**, *10*, 891549, <https://doi.org/10.3389/fbioe.2022.891549>.
  54. Ediati, R.; Elfianuari, P.; Santoso, E.; Sulistiono, D.O.; Nadjib, M. Synthesis of MCM-41/ZIF-67 composite for enhanced adsorptive removal of methyl orange in aqueous solution. *In Mesoporous Materials-Properties and Applications*. **2019**, DOI: 10.5772/intechopen.84691.
  55. Butonova, S.A.; Ikonnikova, E.V.; Sharshheeva, A.; Chernyshov, I.Y.; Kuchur, O.A.; Mukhin, I.S.; Hey-Hawkins, E.; Vinogradov, A.V.; Morozov, M.I. Degradation kinetic study of ZIF-8 microcrystals with and without the presence of lactic acid. *RSC Adv.* **2021**, *11*, 39169-39176, <https://doi.org/10.1039/D1RA07089D>.
  56. Tran, H.N.; Nguyen, N.B.; Ly, N.H.; Joo, S.-W.; Vasseghian, Y. Core-shell Au@ZIF-67-based pollutant monitoring of thiram and carbendazim pesticides. *Environ. Pollut.* **2023**, *317*, 120775, <https://doi.org/10.1016/j.envpol.2022.120775>.
  57. Sadiq, S.; Khan, I.; Humayun, M.; Wu, P.; Khan, A.; Khan, S.; Khan, A.; Khan, S.; Alanazi, A.F.; Bououdina, M. Synthesis of Metal-organic framework-based ZIF-8@ZIF-67 nanocomposites for antibiotic decomposition and antibacterial activities. *ACS Omega* **2023**, *8*, 49244-49258, <https://doi.org/10.1021/acsomega.3c07606>.
  58. Chen, Y.; Zhang, X.; Dong, M.; Wu, Y.; Zheng, G.; Huang, J.; Guan, X.; Zheng, X. MCM-41 immobilized 12-silicotungstic acid mesoporous materials: Structural and catalytic properties for esterification of levulinic acid and oleic acid. *J. Taiwan Inst. Chem. Eng.* **2016**, *61*, 147-155, <https://doi.org/10.1016/j.jtice.2015.12.005>.
  59. Gao, K.; Li, J.; Zhang, T.; Chen, M.; Jin, Y.; Ma, Y.; Ou, G. The hierarchically nitrogenous magnetic porous carbon prepared by ZIF-67 through mesoporous silica-protected calcination for rapid Cr(VI)

- removal. *Microporous Mesoporous Mater.* **2022**, *329*, 111517, <https://doi.org/10.1016/j.micromeso.2021.111517>.
60. Xue, D.; Tang, J.; Zhang, J.; Liu, H.; Gu, C.; Zhou, X.; Jiang, T.; Shi, L. Construction of composite SERS substrate based on black phosphorus/mesoporous ZIF-67 and its selective monitoring of food additives. *Appl. Surf. Sci.* **2024**, *661*, 160001, <https://doi.org/10.1016/j.apsusc.2024.160001>.
61. Khan, S.; Noor, T.; Iqbal, N.; Pervaiz, E.; Yaqoob, L. A zeolitic imidazolate framework (ZIF-67) and graphitic carbon nitride (g-C<sub>3</sub>N<sub>4</sub>) composite based efficient electrocatalyst for overall water-splitting reaction. *RSC Adv.* **2023**, *13*, 24973-24987, <https://doi.org/10.1039/D3RA04783K>.
62. Hu, Y.; Song, X.; Zheng, Q.; Wang, J.; Pei, J. Zeolitic imidazolate framework-67 for shape stabilization and enhanced thermal stability of paraffin-based phase change materials. *RSC Adv.* **2019**, *9*, 9962-9967, <https://doi.org/10.1039/C9RA00874H>.
63. Guerreiro, A.N.; Costa, I.B.; Vale, A.B.; Braga, M.H. Distinctive Electric Properties of Group 14 Oxides: SiO<sub>2</sub>, SiO, and SnO<sub>2</sub>. *Int. J. Mol. Sci.* **2023**, *24*, 15985, <https://doi.org/10.3390/ijms242115985>.
64. Shahmansoori, M.; Yaghmaei, S.; Mahmoodi, N.M. Green synthesis of chitosan-ZIF67 composite beads for efficient removal of malachite green and tetracycline. *Chem. Eng. Sci.* **2025**, *304*, 121017, <https://doi.org/10.1016/j.ces.2024.121017>.
65. Ghafoor, M.; Khan, Z.U.; Nawaz, M.H.; Akhtar, N.; Rahim, A.; Riaz, S. In-situ synthesized ZIF-67 graphene oxide (ZIF-67/GO) nanocomposite for efficient individual and simultaneous detection of heavy metal ions. *Environ. Monit. Assess.* **2023**, *195*, 423, <https://doi.org/10.1007/s10661-023-10966-8>.
66. Mane, P.V.; Rego, R.M.; Yap, P.L.; Losic, D.; Kurkuri, M.D. Unveiling cutting-edge advances in high surface area porous materials for the efficient removal of toxic metal ions from water. *Prog. Mater. Sci.* **2024**, *146*, 101314, <https://doi.org/10.1016/j.pmatsci.2024.101314>.
67. Ibrar, S.; Ali, N.Z.; Ojegu, E.O.; Odia, O.B.; Ikhiya, I.L.; Ahmad, I. Assessing high-performance energy storage of the synthesized ZIF-8 and ZIF-67. *J. Appl. Organomet. Chem.* **2023**, *3*, 294-307, <https://doi.org/10.48309/JAOC.2023.421600.1128>.
68. Saghir, S.; Xiao, Z. Synthesis of novel Ag@ZIF-67 rhombic dodecahedron for enhanced adsorptive removal of antibiotic and organic dye. *J. Mol. Liq.* **2021**, *328*, 115323, <https://doi.org/10.1016/j.molliq.2021.115323>.
69. Mphuthi, L.E.; Erasmus, E.; Langner, E.H.G. Metal Exchange of ZIF-8 and ZIF-67 nanoparticles with Fe(II) for enhanced photocatalytic performance. *ACS Omega* **2021**, *6*, 31632-31645, <https://doi.org/10.1021/acsomega.1c04142>.
70. Qin, J.; Wang, S.; Wang, X. Visible-light reduction CO<sub>2</sub> with dodecahedral zeolitic imidazolate framework ZIF-67 as an efficient co-catalyst. *Appl. Catal. B Environ.* **2021**, *209*, 476-482, <https://doi.org/10.1016/j.apcatb.2017.03.018>.
71. Niazi, L.; Lashanizadegan, A.; Sharififard, H. Chestnut oak shells activated carbon: Preparation, characterization and application for Cr (VI) removal from dilute aqueous solutions. *J. Clean. Prod.* **2018**, *185*, 554-561, <https://doi.org/10.1016/j.jclepro.2018.03.026>.
72. Liu, Y.; Gonçalves, A.A.S.; Zhou, Y.; Jaroniec, M. Importance of surface modification of  $\gamma$ -alumina in creating its nanostructured composites with zeolitic imidazolate framework ZIF-67. *J. Colloid Interface Sci.* **2018**, *526*, 497-504, <https://doi.org/10.1016/j.jcis.2018.05.008>.
73. Nazir, M.A.; Najam, T.; Shahzad, K.; Wattoo, M.A.; Hussain, T.; Tufail, M.K.; Shah, S.S.A.; Rehman, A.u. Heterointerface engineering of water stable ZIF-8@ZIF-67: Adsorption of rhodamine B from water. *Surf. Interfaces* **2022**, *34*, 102324, <https://doi.org/10.1016/j.surfin.2022.102324>.
74. Wang, C.-Y.; Chou, C.-M.; Tseng, P.-S.; Tsao, C.-S. Pore morphology and topology of zeolite imidazolate framework ZIF-67 revealed by small-angle X-ray scattering. *J. Chin. Chem. Soc.* **2021**, *68*, 500-506, <https://doi.org/10.1002/jccs.202000561>.
75. Lei, Y.; Yang, H.; Xie, J.; Chen, Q.; Quan, W.; Wang, A. Synthesis of strong magnetic response ZIF-67 for rapid adsorption of Cu<sup>2+</sup>. *Front. Chem.* **2023**, *11*, 1135193, <https://doi.org/10.3389/fchem.2023.1135193>.
76. Hu, X.; Yan, X.; Zhou, M.; Komarneni, S. One-step synthesis of nanostructured mesoporous ZIF-8/silica composites. *Microporous Mesoporous Mater.* **2016**, *219*, 311-316, <https://doi.org/10.1016/j.micromeso.2015.06.046>.

77. Li, G.; Zhang, H.; Yu, X.; Lei, Z.; Yin, F.; He, X. Highly efficient Co/NC catalyst derived from ZIF-67 for hydrogen generation through ammonia decomposition. *Int. J. Hydrogen Energy* **2022**, *47*, 12882-12892, <https://doi.org/10.1016/j.ijhydene.2022.02.046>.
78. Zhang, M.; Shan, Y.; Kong, Q.; Pang, H. Applications of metal–organic framework–graphene composite materials in electrochemical energy storage. *FlatChem* **2022**, *32*, 100332, <https://doi.org/10.1016/j.flatc.2021.100332>.
79. Muthukumar, C.; Alam, S.; Iype, E.; B.G, P.K. Statistical analysis of photodegradation of methylene blue dye under natural sunlight. *Opt. Mater.* **2021**, *122*, 111809, <https://doi.org/10.1016/j.optmat.2021.111809>.
80. Guan, W.; Gao, X.; Ji, G.; Xing, Y.; Du, C.; Liu, Z. Fabrication of a magnetic nanocomposite photocatalysts Fe<sub>3</sub>O<sub>4</sub>@ZIF-67 for degradation of dyes in water under visible light irradiation. *J. Solid State Chem.* **2017**, *255*, 150-156, <https://doi.org/10.1016/j.jssc.2017.08.012>.
81. Tong, L.; Li, Z.; Ma, Y.; Zhao, L. Synthesis of CeO<sub>2</sub>-loaded composite catalysts of ZIF-67 for activation of persulfate degradation of Congo red dye. *Colloids Surf. A: Physicochem. Eng. Asp.* **2024**, *685*, 133189, <https://doi.org/10.1016/j.colsurfa.2024.133189>.
82. A, H.; M, M.; C, P.P.; G, G.; K, K.M.; Murali, M.; Raghunandan, R. Facile room temperature synthesis of ZIF-67 for efficient photocatalytic degradation of methylene blue under sunlight irradiation. *Ionics* **2024**, *30*, 4917-4930, <https://doi.org/10.1007/s11581-024-05601-6>.
83. Batool, I.; Aroob, S.; Anwar, F.; Taj, M.B.; Baamer, D.F.; Almasoudi, A.; Ali, O.M.; Aldahiri, R.H.; Alsulami, F.M.H.; Khan, M.I.; Nawaz, A.; Maseeh, I.; Nazir, M.K.; Carabineiro, S.A.C.; Shanableh, A.; Fernandez-Garcia, J. Synergistic effect of NiAl-layered double hydroxide and Cu-MOF for the enhanced photocatalytic degradation of methyl orange and antibacterial properties. *Catalysts* **2024**, *14*, 719, <https://doi.org/10.3390/catal14100719>.

## Publisher's Note & Disclaimer

The statements, opinions, and data presented in this publication are solely those of the individual author(s) and contributor(s) and do not necessarily reflect the views of the publisher and/or the editor(s). The publisher and/or the editor(s) disclaim any responsibility for the accuracy, completeness, or reliability of the content. Neither the publisher nor the editor(s) assume any legal liability for any errors, omissions, or consequences arising from the use of the information presented in this publication. Furthermore, the publisher and/or the editor(s) disclaim any liability for any injury, damage, or loss to persons or property that may result from the use of any ideas, methods, instructions, or products mentioned in the content. Readers are encouraged to independently verify any information before relying on it, and the publisher assumes no responsibility for any consequences arising from the use of materials contained in this publication.

## Supplementary materials

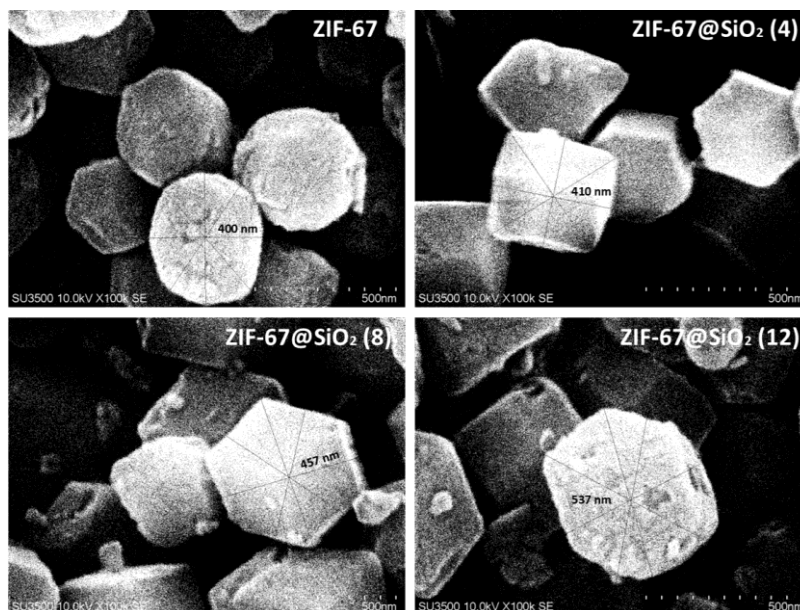


**Figure S1.** SEM Micrograph of ZIF-67 and ZIF-67@SiO<sub>2</sub> with percentage mass silica.

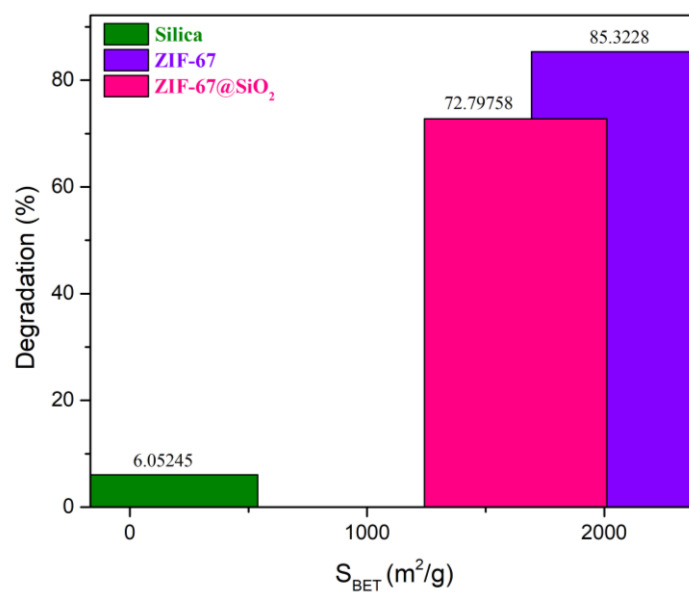


**Figure S2.** Surface Area correlates with photocatalytic performance.

**Table S1.** EDS analysis of the sample.

Element (% weight)	Sample			
	ZIF-67	ZIF-67@SiO <sub>2</sub> (4)	ZIF-67@SiO <sub>2</sub> (8)	ZIF-67@SiO <sub>2</sub> (12)
C	62,27	45,11	33,83	59,97
N	20,13	23,96	17,15	21,12
O	4,38	1,78	1,45	4,85
Co	13,23	28,81	47,00	13,53
Si	-	0,27	0,57	0,51

**Table S2.** ANOVA One Way Photodegradation CGR.

Source	Sum of Squares	Degrees of Freedom	Mean Squares	F-value	P-value
Between Groups	8733.69761	1	8733.69761	17.78365	0.002928
Within Groups	3928.865434	8	491.1081792		
Total	12662.56304	9			